Available online at www.sciencedirect.com
SCIENCE DIRECT®
Journal of Solid State Chemistry 178 (2005) 2575–2585
JOURNAL OF SOLID STATE CHEMISTRY
www.elsevier.com/locate/jssc

High-resolution X-ray diffraction, DIFFaX, NMR and first principles study of disorder in the Li_2MnO_3–$Li[Ni_{1/2}Mn_{1/2}]O_2$ solid solution

Julien Bréger[a], Meng Jiang[a], Nicolas Dupré[a], Ying S. Meng[b,c], Yang Shao-Horn[c], Gerbrand Ceder[c], Clare P. Grey[a,*]

[a]*Department of Chemistry, SUNY Stony Brook, Stony Brook, NY 11794-3400, USA*
[b]*Advanced Materials for Micro- & Nano-Systems, Singapore-MIT Alliance, Singapore 117576*
[c]*Massachusetts Institute of Technology, Cambridge, MA 02139, USA*

Received 5 March 2005; received in revised form 11 May 2005; accepted 12 May 2005
Available online 14 July 2005

Abstract

X-ray diffraction patterns of $Li[Li_{(1-2x)/3}Ni_xMn_{2/3-x/3}]O_2$ show reflections between 20° and 35°, 2θ (Cu$K\alpha$) due to Li_2MnO_3-like ordering of the transition metal (Ni, Mn and Li) layers. The ordering is rarely perfect, resulting in characteristic broadening and changes in the intensities of these reflections. ^{6}Li MAS NMR studies of Li_2MnO_3 show that the $[Li_{1/3}Mn_{2/3}]$ layers are well ordered, the disorder arising from the stacking of the layers in the *c*-direction. DIFFaX was used to model the Li_2MnO_3 XRD data and extract the stacking fault frequency. The results show that even well-ordered cation layers may show only weak or no superstructure reflections, if there is no or little ordering in the *c*-direction.
© 2005 Elsevier Inc. All rights reserved.

Keywords: Li-ion batteries; Solid-state NMR; Layered compounds; Stacking faults; Ordering; X-ray diffraction

1. Introduction

$Li[Ni_xLi_{1/3-2x/3}Mn_{2/3-x/3}]O_2$ materials have been widely investigated over the last 3 years due to their high capacities and good cycle life when used as positive electrodes in lithium rechargeable batteries. Ohzuku et al. [1] reported that $Li[Ni_{1/2}Mn_{1/2}]O_2$ prepared at 1000 °C can deliver a very high capacity of 200 mAh/g between 2.5 and 4.5 V while Lu et al. [2] reported that a material, with the same nominal composition, gives a capacity of 160 mAh/g when the cycling process is performed between 2.0 and 4.6 V. All these materials are derived from the ordered rock-salt structure of α-$NaFeO_2$ and are structurally related to $LiCoO_2$. The composition $Li[Ni_xLi_{1/3-2x/3}Mn_{2/3-x/3}]O_2$ can be viewed as a solid solution between the two end members, Li_2MnO_3, and $Li[Ni_{1/2}Mn_{1/2}]O_2$. $Li[Ni_{1/2}Mn_{1/2}]O_2$ adopts an $R\bar{3}m$ space group and consists of "Li" layers containing approximately 90% Li^+ and 10% Ni^{2+} ions, and "transition metal" layers with Ni^{2+}, Mn^{4+} and some Li^+ ions [3,4]. Li_2MnO_3 may be rewritten as $Li[Li_{1/3}Mn_{2/3}]O_2$ in the notation used to describe many of these layered materials. The "transition metal" layer now comprises Li and Mn ions in an atomic ratio for Li:Mn of 1:2, arranged to form a "honey-comb" ordering scheme (Fig. 1a). This reduces the symmetry of Li_2MnO_3 and results in superstructure peaks between 20° and 35°, 2θ (Cu$K\alpha_1$) in the X-ray diffraction (XRD) pattern [5,6]. XRD patterns of $Li[Ni_xLi_{1/3-2x/3}Mn_{2/3-x/3}]O_2$ with intermediate values of x (e.g., $x = 1/9$, $1/3$, $1/6$) also show superstructure reflections consistent with Li_2MnO_3-type ordering and electron diffraction patterns [7,8] of $Li[Ni_{1/2}Mn_{1/2}]O_2$ show superstructure

*Corresponding author. Fax: +631 632 5731.
E-mail address: cgrey@notes.cc.sunysb.edu (C.P. Grey).

0022-4596/$ - see front matter © 2005 Elsevier Inc. All rights reserved.
doi:10.1016/j.jssc.2005.05.027

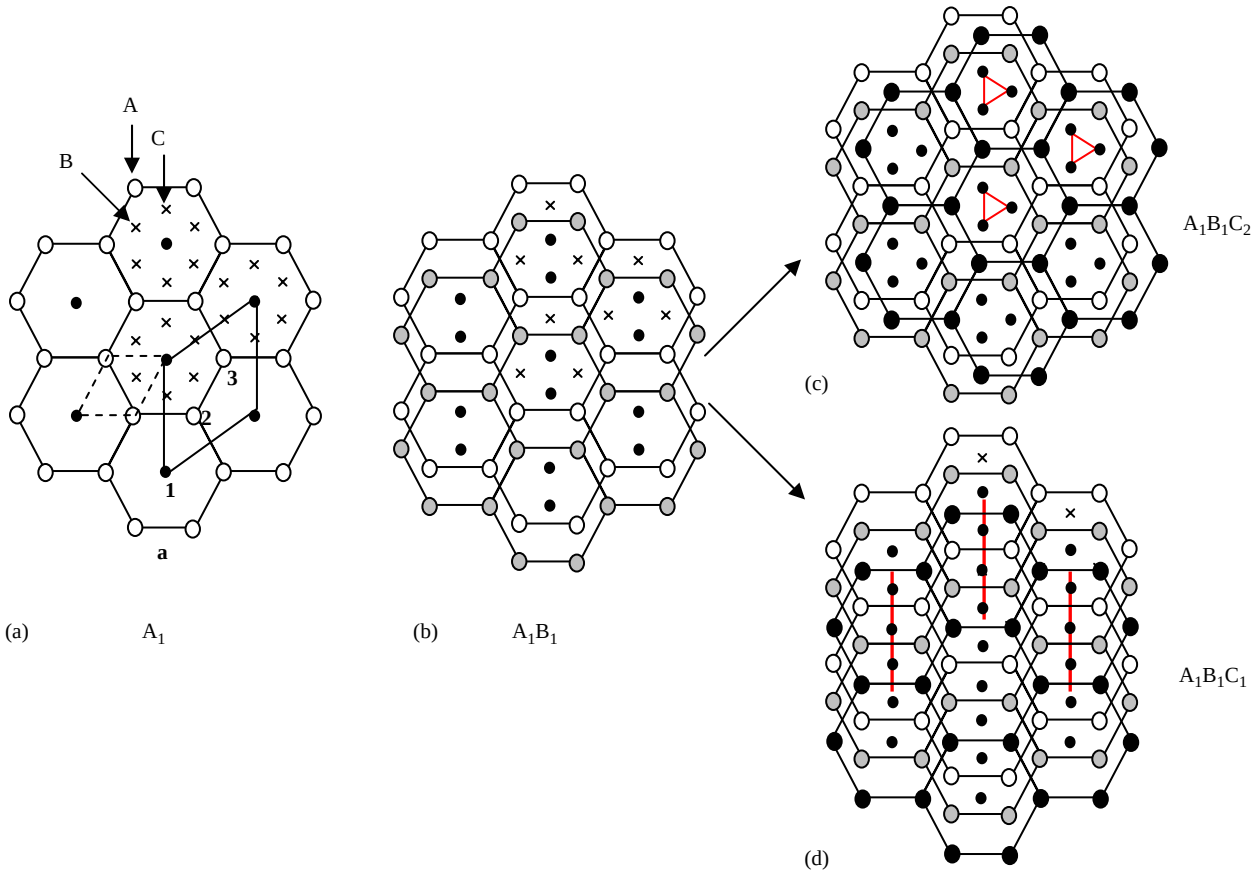

Fig. 1. Schemes generated by stacking "honey-comb" layers. (a) The first "honey-comb" $Li_{1/3}Mn_{2/3}$ layer, A_1. The Mn and Li ions are denoted by white and black (smaller) circles, respectively. The crosses represent the locations in the *ab*-planes of the *B* and *C* holes in a close-packed array. The enlarged $3^{1/2}a \times 3^{1/2}a$ unit cell is shown along with the locations of three different atoms in this cell. The α-$NaFeO_2$ unit cell is also shown in dashed lines. (b) The addition of a second layer (gray and black circles), to generate A_1B_1 stacking. Two possibilities for the addition of the third layer (black circles) are possible, generating (c) a 3-fold screw axis (triangles), for $P3_112$ stacking ($A_1B_1C_2$) and (d) mirror planes (lines) for the $C2/m$ stacking ($A_1B_1C_1$).

peaks consistent with long-range ordering of the cations in the transition metal layers. In order to understand the ordering in the transition metal layers in the $Li[Ni_xLi_{1/3-2x/3}Mn_{2/3-x/3}]O_2$ series, we have chosen, in the work presented in this paper, to investigate the ordering in the end member Li_2MnO_3 in some detail.

How the ordered transition metal layers are stacked in Li_2MnO_3 is still controversial. Different stacking configurations were previously proposed in literature, one resulting in the $C2/c$ space group (Jansen, 1973; Riou, 1992) [9,10] and another resulting in the $C2/m$ space group (Strobel, 1988; Massarotti, 1997) [5,6]. Recent TEM studies by Meng et al. [7] showed that the stacking sequence that results in a $P3_112$ space group also needs to be considered for the other end member $Li[Ni_{0.5}Mn_{0.5}]O_2$. These stacking schemes were proposed by Lang in as early as 1966 [11]. Fig. 1 shows two different ways of stacking the honey-comb ordered ($Li_{1/3}Mn_{2/3}$) layers (containing Li atoms surrounded by 6 Mn atoms in the *ab* plane) along the *c*-axis, to generate $C2/m - A_1B_1C_1$ and $P3_112 - A_1B_1C_2$ stacking. All structures derived from α-$NaFeO_2$ (i.e., O3 packing) contain *ABCABC* stacking of the $Li_{1/3}Mn_{2/3}$ layers (Fig. 1) in the *c*-direction. Thus, each layer (or 2D net) is labeled *A*, *B* or *C*, denoting the position of the cations in the close packed layers. Honey-comb ordering results in an enlargement of the α-$NaFeO_2$ cell in the *a*–*b* plane to form a $3^{1/2}a \times 3^{1/2}a$ cell, where *a* is the cell parameter of the α-$NaFeO_2$ cell, and there are now three atoms per unit cell in the 2D net. This generates three possible 2D nets, A_1, A_2 or A_3, the subscript labeling the position of the Li ions in the unit cell (Fig. 1(a)). Starting with the A_1 net, a second net may then be placed above this to generate the arrangement A_1B_1 (Fig. 1(b)). The other possible arrangements, A_1B_2 and A_1B_3, are related to A_1B_1 by a 120° rotation and so are not unique. There are then two possibilities for the addition of a third net, generating either $A_1B_1C_1$ or $A_1B_1C_2$ stacking. $A_1B_1C_2A_1B_1C_2\ldots$ stacking results in a 3-fold screw axis along the *c*-axis and the space group $P3_112$, while

stacking involving the $A_1B_1C_1$ blocks results in the $C2/m$ structure. Fig. 2 illustrates how the monoclinic $C2/m$ unit cell [5] can be redrawn as a larger hexagonal unit cell, which is identical in size to that found for $P3_112$ stacking, allowing easy comparison between these two structures. More complicated stacking schemes are possible if the 3-layer blocks are combined with different ones. For example, the stacking block $A_1B_1C_2$ can be combined with an $A_2B_3C_1$ block, to form the six-layer repeat sequence $A_1B_1C_2A_2B_3C_1$. This stacking scheme results in the $C2/c$ space group proposed by some authors for Li_2MnO_3 [9,10]. These stacking schemes have been found in other materials including Li_2SnO_3 and Li_2IrO_3 [9,11,12].

Clearly, many stacking schemes are possible for Li_2MnO_3 and related structures. The differences in energies between these schemes may not be large, since these layers are separated by three other (oxygen and lithium) layers, and intergrowths between these structures may be possible. The purpose of this paper is to

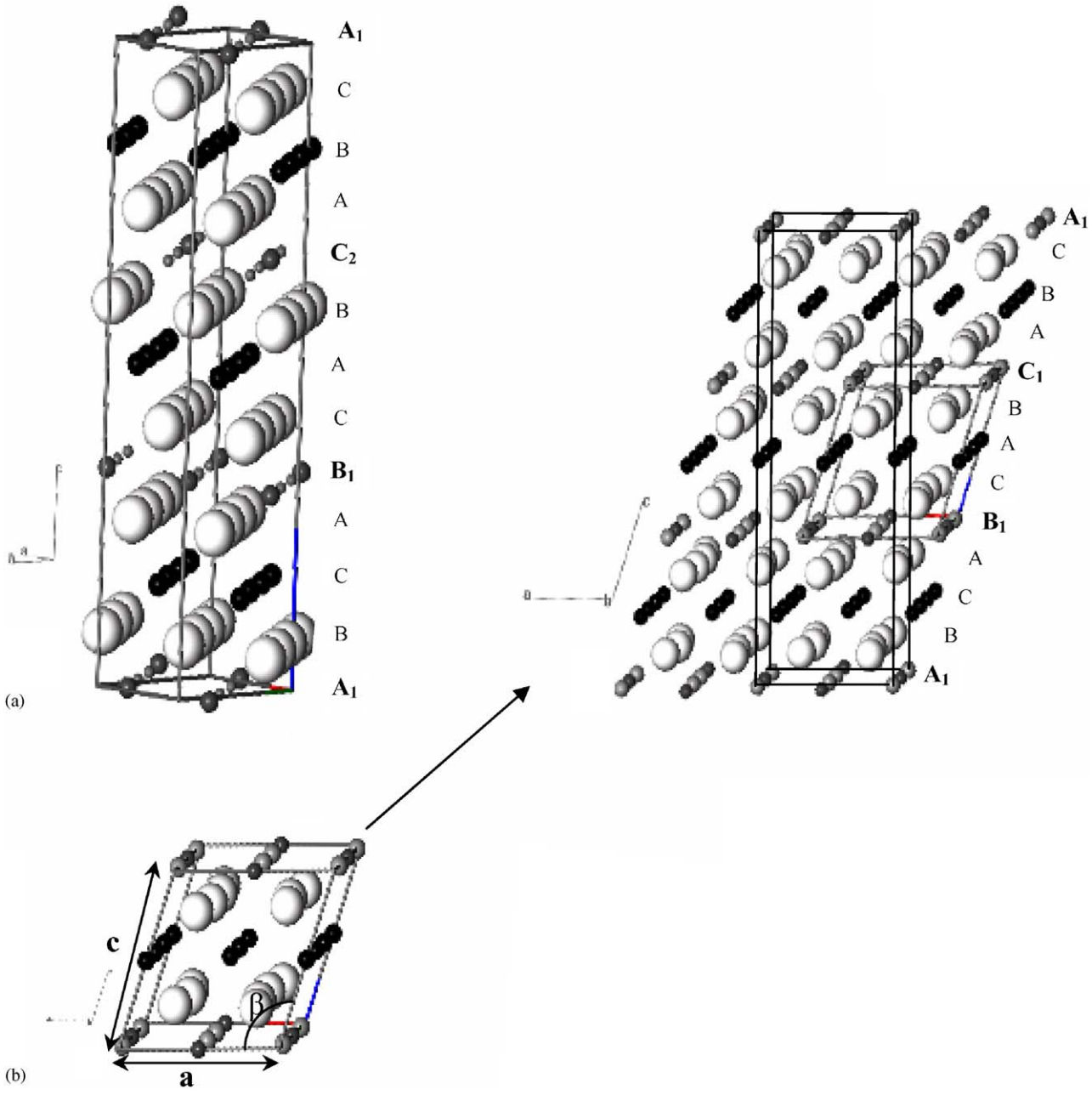

Fig. 2. Two different unit cells generated by stacking honey-comb layers. (a) $P3_112$ and (b) $C2/m$ unit cells; (c) the $C2/m$ unit cell may be redrawn as a larger, hexagonal cell, for a value of β for the monoclinic cell equal to π-$\cos^{-1}(a/3c)$. The O and Mn atoms are represented by white and light gray spheres, respectively. The Li in Li layers and transition metal layers are represented by black and dark gray spheres, respectively.

explore the effect on the XRD patterns of these materials of stacking faults of these layers along the *c*-axis, as a function of different heat treatments. DIFFaX [13] simulations are used to model these faults and ^{6}Li MAS NMR spectroscopy is used to investigate the local structure in these materials. In addition, first principles calculations are used to estimate the energy differences between different stacking sequences.

2. Experimental

2.1. Synthesis

Stoichiometric amounts of Li_2CO_3 and Mn_2O_3 were mixed and fired at 650 °C for 12 h to remove the CO_2. The mixture was then heated at either 850 °C for 24 h or at 1000 °C for 1 month, and then slowly cooled to room temperature at a rate of 1 °C/min. These samples are referred to as Li_2MnO_3-850-1d and Li_2MnO_3-1000-1m, respectively. $Li[Ni_{1/2}Mn_{1/2}]O_2$ and $Li[Li_{1/9}Ni_{1/3}Mn_{5/9}]O_2$ powders were prepared by the double-mixed hydroxide method [1,2]. An aqueous solution of stoichiometric amounts of transition metal nitrates was prepared, which was slowly dripped (1–2 h) into 400 mL of a stirred solution of LiOH using a burette, yielding a precipitate of $M(OH)_2$, where $M = Mn$ and Ni, with a homogeneous cation distribution. The dried precipitate was mixed with $Li(OH) \cdot H_2O$ in stoichiometric proportions. The mixture was then heated in air at 480 °C for 12 h, and at 1000 °C for 3 days and slowly cooled at room temperature at a rate of 1 °C/min. These samples are referred to as $Ni_{1/2}$-1000-3d and $Ni_{1/3}$-1000-3d, for $Li[Ni_{1/2}Mn_{1/2}]O_2$ and $Li[Li_{1/9}Ni_{1/3}Mn_{5/9}]O_2$, respectively, according to their Ni content and heating procedures.

2.2. XRD

High-resolution synchrotron XRD of $Li[Ni_{1/2}Mn_{1/2}]O_2$, $Li[Li_{1/9}Ni_{1/3}Mn_{5/9}]O_2$ and Li_2MnO_3 were collected by Peter L. Lee at the 32-ID beamline at the Advanced Photon Source (APS), Argonne National Laboratories ($\lambda = 0.4958$ Å). XRD simulations were performed with the program DIFFaX (written by Newsam and Treacy [13]), in order to model stacking faults along the *c*-axis. For clarity, the 2θ values in all the plots were converted so as to correspond to those seen for Cu$K\alpha_1$ wavelengths ($\lambda = 1.5406$ Å).

2.3. NMR

To probe the local environment of Li atoms in Li_2MnO_3, ^{6}Li MAS NMR experiments were performed on the two Li_2MnO_3 samples at an operating frequency of 29.47 MHz on a CMX-200 spectrometer. A 2 mm double resonance probe built by Samoson and co-workers was used to achieve a 38 kHz spinning speed. All spectra were acquired with a rotor synchronized echo pulse sequence (90°-τ-180°-τ-acq), where $\tau = 1/\nu_r$. $\pi/2$ pulse widths of 3.5 μs were used with pulse delays of 0.2 s. The spectra were acquired at "room temperature" (i.e., the spectra were acquired with no control of the temperature), which corresponds to a sample temperature of between 70 and 80 °C.

2.4. Computations

First principles computations on the $C2/m$, $P3_112$, and $C2/c$ stackings were performed in the Generalized Gradient Approximation to Density Functional Theory as implemented in VASP. Ultrasoft GGA pseudopotentials were used, with Perdew–Wang exchange correlation functions (PW-GGA). As the energy differences between these structures are extremely small, dense *k*-point meshes were used for the Brillouin zone integrations.

3. Results

3.1. XRD

Fig. 3 shows the XRD patterns of Li_2MnO_3-850-1d, Li_2MnO_3-1000-1m, $Ni_{1/2}$-1000-3d and $Ni_{1/3}$-1000-3d. As shown in the enlargement in Fig. 3II, both Li_2MnO_3 samples exhibit very similar patterns, except for noticeable differences in the linewidths and intensities of the reflections in the 20–35°, 2θ region. The peak broadening decreases on longer heat treatment at higher temperature, and the pattern is closer to that reported in the literature. Nonetheless, all the reflections can be indexed with the $C2/m$ structure (as proposed by Strobel et al. [6]). All the peaks in the 20–35°, 2θ region are completely absent for the α-$NaFeO_2$ structure, with the $R\bar{3}m$ space group; these "superstructure" peaks result from the ordering of the Li/Mn ions in the *a*–*b* planes. Similar XRD patterns are seen for $Li[Ni_{1/2}Mn_{1/2}]O_2$ and $Li[Li_{1/9}Ni_{1/3}Mn_{5/9}]O_2$, samples, although the superstructure peaks in the 20–35°, 2θ region are weaker, especially for the $x = 0.5$ sample. The presence of the superstructure peaks is consistent with the NMR spectra of these materials, where resonances due to Li surrounded by five or six Mn ions in the transition metal (Mn/Ni/Li) layer are seen [14].

Many of the reflections between 44° and 65°, 2θ show splittings in the pattern of the sample of Li_2MnO_3 annealed for a month. The same reflections are broadened in the patterns of Li_2MnO_3-850-1d and $Ni_{1/3}$-1000-3d, but individual reflections cannot be resolved. These reflections can only be indexed with a $C2/m$ space group and not with the $P3_112$ space group. For

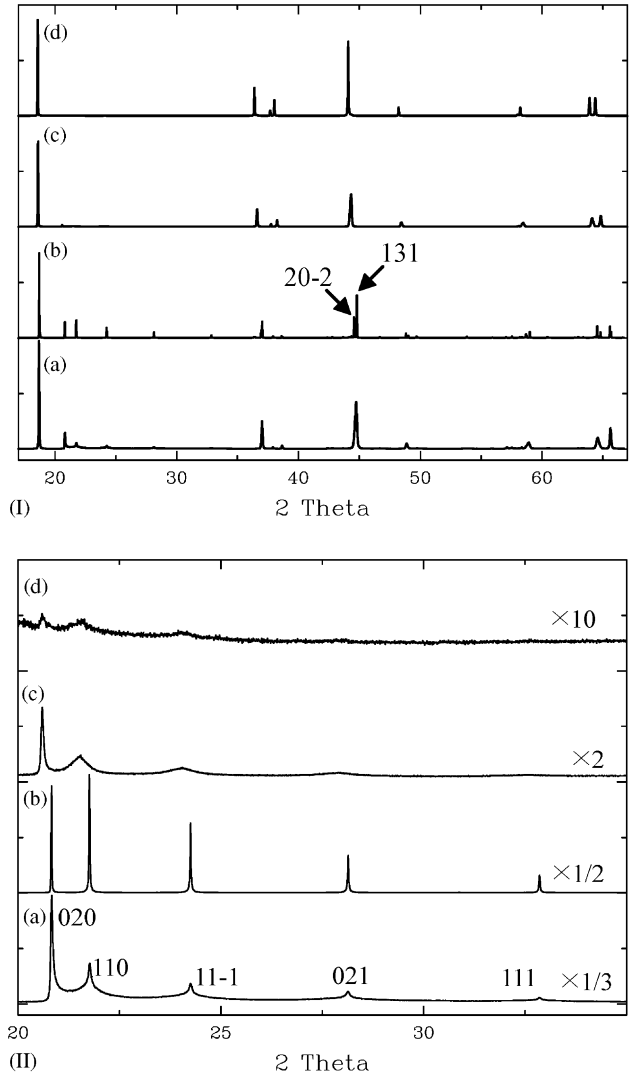

Fig. 3. XRD patterns of (I): (a) Li_2MnO_3-850 °C-1d, (b) Li_2MnO_3-1000 °C-1m, (c) $Li[Li_{1/9}Ni_{1/3}Mn_{5/9}]O_2$-1000 °C-3d, and (d) $Li[Ni_{1/2}Mn_{1/2}]O_2$-1000 °C-3d. These experimental patterns were collected at the APS (32-ID) with $\lambda = 0.4958$ Å. For clarity, the 2θ values were changed to correspond to those for Cu$K\alpha_1$ X-ray irradiation ($\lambda = 1.5406$ Å). (II): Enlargements of the XRD patterns of the four samples with the 2θ range between 20° and 35°. The peaks were indexed with the $C2/m$ space group.

example, the two reflections at approx. 44.5°, 2θ are assigned to the $20\bar{2}$ and 131 reflections of the $C2/m$ cell. The size of the splittings is related to the value of β in the monoclinic cell. For example, for a value of β equal to $(180°-\cos^{-1}(a/3c))$, where a and c are the cell parameters of the $C2/m$ monoclinic cell, no splitting is observed and the $C2/m$ cell may be redrawn as shown in Fig. 2(b), as a hexagonal cell. In this case, it would be difficult to distinguish between the $C2/m$ and $P3_112$ cells, without further profile refinement. However, the observation of splitting provides clear evidence for a monoclinic distortion of the cell, and thus the $P3_112$ space group can be rejected for the ordered compound.

3.2. NMR

Fig. 4 shows the ^{6}Li MAS NMR spectra of Li_2MnO_3-1000-1m and -850-1d. Two sets of isotropic resonances, at approx. 750 and 1510 ppm, are observed for both sets of materials, which can be assigned to Li ions in the Li layers and transition metal layers, respectively, based on the relative intensities of the resonances and their Fermi-contact shifts [15–17]. More careful examination of the spectra reveals that the peak at approx. 750 ppm in a spectrum of Li_2MnO_3-1000-1m is split into two resonances at 775 and 759 ppm with approximate intensities of 1:2, while a whole series of resonances are observed for the -850-1d, sample indicating that there are a wide range of different local environments for Li in the Li layers.

3.3. Calculations

The first principles results give very small energy differences between the $C2/m$, $P3_112$, and $C2/c$ stackings, though $C2/m$ consistently has the lowest energy for calculations with high k-point density. The $C2/c$ structure is about 2 MeV per formula unit higher in energy than the $C2/m$ structure, while $P3_112$ is approximately 1 MeV higher in energy than $C2/m$. While these numbers are small, we believe they are numerically significant.

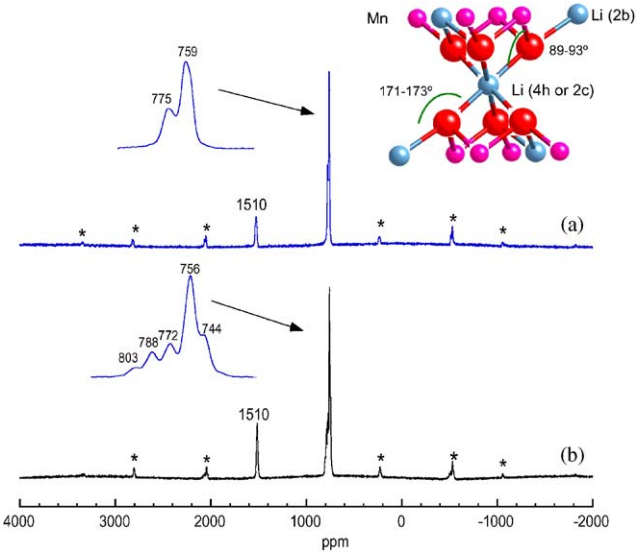

Fig. 4. ^{6}Li MAS NMR spectra of (a) Li_2MnO_3-1000-1m and (b) Li_2MnO_3-850-1d. The isotropic resonances are labeled with their corresponding shifts; the remaining peaks are spinning sidebands, which are marked with *. The inserts on the left are enlargements of the peaks at approx. 750 ppm. The insert on the right shows the local environment for the Li ions in the Li layers.

4. Discussion

4.1. Implications from the probe of short-range order, NMR

Each Li ion in the $Li_{1/3}Mn_{2/3}$ honey-comb layer is surrounded by six Mn ions in its first coordination shell; this corresponds to the 2*b* crystallographic site in the $C2/m$ structure. A Fermi contact (hyperfine) shift of 1500 ppm is predicted for this local environment, based on Li–O–Mn bond angles for this environment (close to 90°). No evidence for any disorder of the honey-comb layers is seen. Any Li–Mn site exchange will result in Li local environments containing fewer Mn^{4+} ions. For example, interchanging one set of Li and Mn ions in an adjacent Li–Mn pair will result in three new Li local environments, one nearby only four Mn and two nearby five Mn ions. These local environments will resonate at approx. 1250 and 1000 ppm, respectively. No resonances are seen in this shift range for both samples. Random occupancy of 1% of the Li ions on the Mn site, and 0.05% of the total Mn content on the Li sites, results in local environments $Li(Mn)_n$, $n = 6$, 5, 4, 3 with concentrations of 92.3%, 5.6%, 0.3%, and 1.8%. (These local environments also contain six Li ions from the Li layers, but since only the Mn^{4+} ions give rise to large (hyperfine) shifts we shall ignore these ions in the subsequent discussion.) Our signal-to-noise (0.4%) is high enough to detect these resonances. Given the signal-to-noise value, we estimate that we should be able to detect levels as low as 0.2% for Li occupancy on the Mn site (where 1% of the Li in the $Li_{1/3}Mn_{2/3}$ layers will be present as $Li(Mn)_5Li$ environments). Thus our NMR results provide strong evidence for long-range ordering of Li and Mn in the honey-comb layers in both samples.

Stacking of two honey-comb layers generates two distinct local environments for the Li in the Li layers (the Li' ions) in between the two honey-comb layers, with a site multiplicity of 1:2. These differ in the arrangements of the Li and Mn in their first and second cation coordination shells. In the A_1B_1 stacking shown in Fig. 1(b), the Li′ ions occupy the "C" positions in the A_1B_1 blocks, indicated by crosses in this figure. These sites correspond to the 2*c* and 4*h* sites in the $C2/m$ structure. The 4*h* and 2*c* Li sites both contain four Mn ions in the first cation coordination shell, with on average eight Li–O–Mn bond angles of 93.1° and 92.5° and four more distant ions (in the second coordination shell) with on average four Li–O–Mn bond angles of 172.8° and 171.3°, respectively (Fig. 4) [5]. (Again, we have ignored the six Li in the first coordination sphere from the Li layers. We have also used the structure of Massaroti et al. [5] to calculate the quoted bond angles; these angles do change significantly when using the values from our structural refinement presented below.) Since Li–O–Mn bond angles closest to 90° result in the largest positive shifts (approx. 250 ppm per Mn^{4+} ion, or 125 ppm per Li–O–Mn connectivity) and angles closest to 180° result in large negative shifts (approx. −70 ppm per Mn^{4+} ion or Li–O–Mn connectivity) [18], the shift for the 4 h site is expected to be slightly smaller than that for the 2*c* site, consistent with the observed shifts seen in Fig. 4a of the intense (759 ppm) and weaker (775 ppm) resonances.

The ^{6}Li MAS NMR spectrum (Fig. 4(b) of Li_2MnO_3-850-1d contains a whole series of resonances at 750–800 ppm. This is not consistent with simple $A_1B_1C_1(C2/m)$ stacking where only two Li′ sites are predicted. Similarly, $A_1B_1C_2(P3_112)$ stacking of ideal layers, where the Li, Mn and O ions all occupy positions on a perfect α-$NaFeO_2$ lattice also generates only two Li sites (all the Li′ layers are equivalent due to the 3_1 axis). The additional resonances must arise from stacking faults or intergrowths of different structures. A Li ion in the A_1B_1 block contains Mn^{4+} ions in its first and second cation coordination shells in the A_1 and B_1 blocks. The closest Mn^{4+} ions in a C_1, C_2 or C_3 layer are more than 7 Å away and are separated by six M–O bonds (M = Li, Mn). It is, therefore, unlikely that the Mn^{4+} ions in the C (C_1, C_2 or C_3) layers produce a significant contribution to the Fermi contact shift. Instead, the differences in shifts most likely arise from small changes in Li–O–Mn bond angles that arise from differences in the stacking. To illustrate this effect, we started with the Li_2MnO_3 $C2/m$ structure and replaced half of the Mn ions by Li and all of the Li ions by Mn in one layer, to generate a fault in the sequence, which can be written as $A_1B_1C_1A_1B_2C_1A_1B_1C_1\ldots$ In order to provide a rough estimate of the shift, we assumed that the M–O bond angles remain unchanged in a stacking fault. In this scenario, the Li′ ions in A_1B_2 blocks will have slightly different Li–O–Mn bonds of 89.4° (×8) and 171.5° (×4) for the first environment and 89.4° (×8) and 172.5° (×4) for the second. Larger shifts than those seen for ordered $C2/m$ environments are predicted for these local environments. Slightly different environments and new resonances are similarly generated for Li′ ions in an A_1B_3 block. Thus, it is clear that even deviations from ideal stacking, caused by stacking faults of transition metal layers, will likely generate small local distortions, resulting in Li′ resonances with slightly different shifts.

4.2. XRD refinements and simulations

Rietveld refinements were performed for the two Li_2MnO_3 samples and are presented here in order to illustrate some of the pitfalls and difficulties associated with the structural refinements of these heavily faulted materials. Fig. 5 shows the attempted Rietveld refinement with GSAS-EXPGUI [19] for the Li_2MnO_3-1000-1m sample. $C2/m$ space group was used and cell

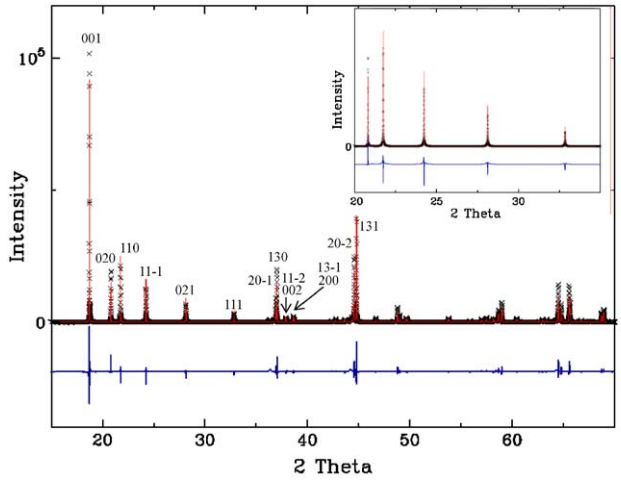

Fig. 5. Rietveld refinement using the XRD pattern ($\lambda = 0.4958$ Å) of Li_2MnO_3-1000-1m. The crosses and the solid line represent the experimental data and the calculated pattern, respectively. The difference between the calculated and experimental patterns is shown below the data. For clarity, the 2θ values were changed to correspond to those for Cu$K\alpha_1$ X-ray irradiation ($\lambda = 1.5406$ Å).

parameters of $a = 4.9303(1)$ Å, $b = 8.5264(1)$ Å, $c = 5.0264(1)$ Å and $\beta = 109.43°$ were found. As discussed above, the $P3_112$ space group does not account for the splitting of some higher-order reflections. Unfortunately, the fit to the profile is poor due to both the differential line broadenings of the reflections, particularly in the 20–35° 2θ region, and the weaker intensities of these peaks in comparison to those predicted for the ideal Li_2MnO_3 structure. Previous workers (e.g., Massarroti et al. [5] for Li_2MnO_3 and Kobayashi et al. [12] for the $C2/c$ structure of Li_2IrO_3) have attempted to improve the fit by introducing Li/Mn exchange between the sites in the honey-comb layers. Li/Mn exchange does indeed result in a slightly improved fit (R_{wp} from 30.6% to 29.7%, R_p from 24.5% to 23.5%). However, the obtained R-factors are still quite high and the profile fit is poor. Most importantly, the NMR spectra provide no evidence for this Li/Mn exchange and, hence, this approach does not appear justified. Attempts were also made to refine the structure of the Li_2MnO_3-850-1d sample, but the obtained Rietveld profile fit was even worse unless the 20–35°, 2θ (Cu$K\alpha_1$) region was excluded. Values of $a = 4.923(3)$ Å, $b = 8.516(4)$ Å, $c = 5.017(2)$ Å and $\beta = 109.25(3)°$ were found with the $C2/m$ space group, along with R-factors of $R_{wp} = 8.9$ and $R_P = 4.9\%$ (for the profiles with the large excluded regions). Although no peak splitting was observed due to the monoclinic distortion, the broadening of certain reflections (e.g., the $20\bar{2}$ and 131 $C2/m$ reflections; 114 and $11\bar{4}$ in the ideal hexagonal $P3_112$ cell) could not be accounted for by using the $P3_112$ cell. The value of β is closer to the ideal value of β (109.1°) than the value of β found for the Li_2MnO_3-1000-1m sample, indicating a smaller monoclinic distortion of the unit cell.

Line broadening of the XRD peaks is most likely due to disorder in the stacking of transition metal layers. This hypothesis was tested by performing simulations of the XRD data with the DIFFaX program [13]. A wavelength of 1.5406 Å and a pseudo-Voigt broadening profile function ($u = 0.1$, $v = -0.1$, $w = 50$ and $\sigma = 0.6$) were used. For convenience, the hexagonal $P3_112$ cell was used in all the simulations. We chose cell parameters of $a = 4.92$ Å and $c = 14.217$ Å, which were obtained by indexing the Li_2MnO_3-1000-1m XRD pattern with the $P3_112$ cell. This cell will not account for the splittings of the higher-order reflections due to the monoclinic distortion.

The unit cell was divided into three layers (A, B and C), each layer consisting of an oxygen, a lithium (Li′), a second oxygen and a honey-comb layer composite block. There are then nine types of layers, (A_i, B_i and C_i, where $i = 1$, 2 or 3), since there are three ways of arranging Li atoms in the honey-comb layers. This notation is identical to that introduced in Fig. 1 to describe the different stacking schemes. Structures are generated in DIFFaX by listing probabilities for a particular sequence of stacking vectors, each vector mapping one layer onto the next. For example, $C2/m$ stacking is generated by setting probabilities P for the stacking vectors, $A_1 \rightarrow B_1$, $B_1 \rightarrow C_1$, and $C_1 \rightarrow A_1$ to one; the probabilities for all other vectors are set to zero. Similarly, $P3_112$ stacking involves setting probabilities of one for the following stacking vectors, $A_1 \rightarrow B_1$, $B_1 \rightarrow C_2$, $C_2 \rightarrow A_1$. A stacking fault is then introduced by setting $P<1$ for some of the vectors. There are a number of different ways of generating faults in the stacking of transition metal layers. The simple $C2/m$ stacking fault $\ldots A_1B_1C_1{-}f{-}A_2B_2C_2$ maintains the monoclinic distortion (Fig. 6(a)), while others involving a rotation of the stacking direction by 120° or 240° will result in loss of the monoclinic distortion (Fig. 6(b) and (c)). Even a simple $C2/m$ "translational" stacking fault [20] ($-f-$) such as $\ldots A_1B_1C_1{-}f{-}A_2B_2C_2\ldots$ requires that we define probabilities P for all the possible stacking vectors, as illustrated in the table provided in the Supplemental material. Figs. 7a and 8a display the XRD simulations for Li_2MnO_3 with varying degrees of stacking faults, and $P3_112$ and $C2/m$ stacking schemes, respectively. Both space groups seem to model the differential broadening, when sufficient stacking faults are introduced.

A concentration of stacking faults of around 5% has to be introduced to model the XRD data if the $P3_112$ model is used, while a higher concentration of around 10% is required for the $C2/m$ model for Li_2MnO_3-850-1d. (10% of stacking faults indicates that a fault occurs on average every 10 [$Li_{1/3}Mn_{2/3}$] layers). In contrast, only around 0.5% for the $P3_112$ model, and 2% of

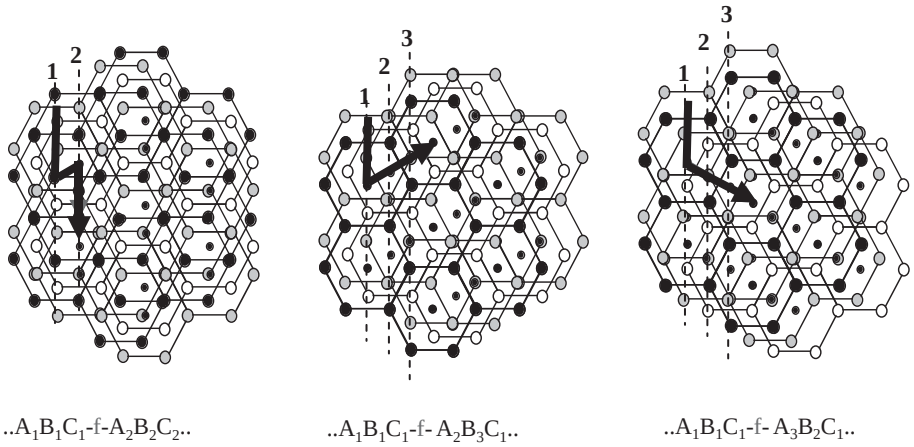

Fig. 6. Examples of $C2/m$-type stacking faults. The arrows indicate the directions of the stacking faults.

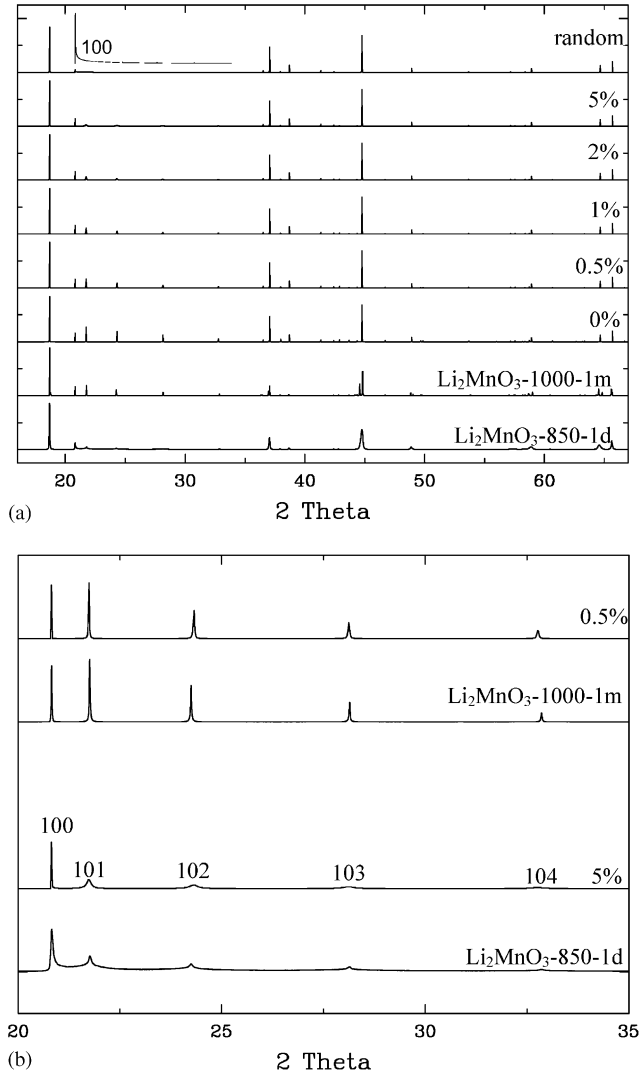

Fig. 7. (a) Comparison between experimental and simulated XRD patterns between 20° and 35° ($\lambda = 1.5406$ Å) of Li_2MnO_3 with $P3_112$ stacking with different percentages of stacking faults. The insert shows an enlargement of the 2θ region near the 1 0 0 reflection for the random stacking profile. (b) Enlargement between 20° and 35°, 2θ showing the best fit between the experimental and simulated data.

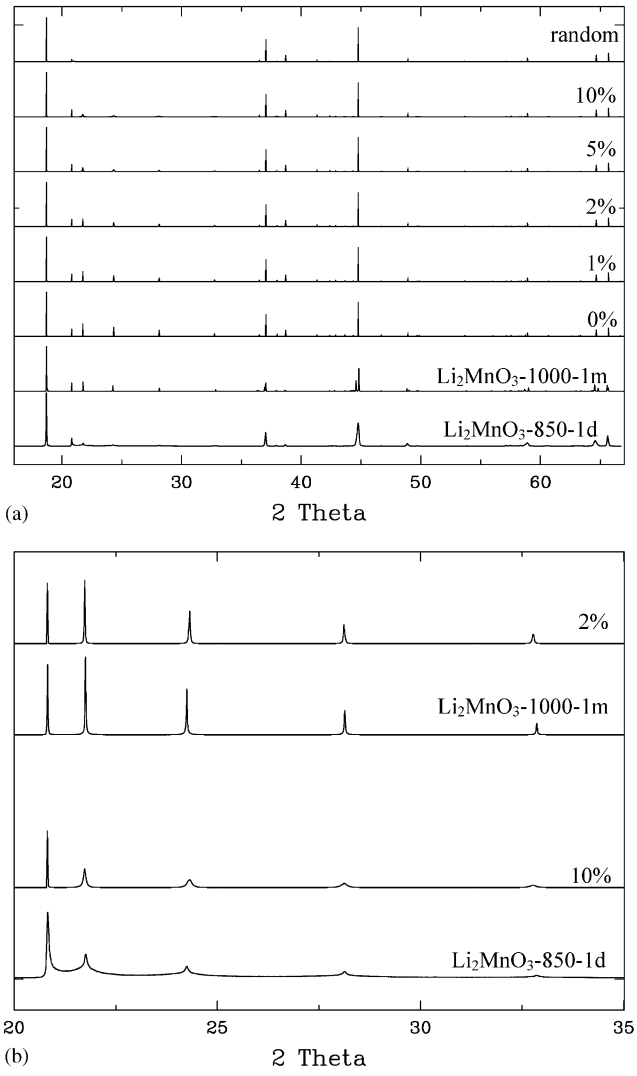

Fig. 8. (a) Comparison between experimental and simulated XRD patterns ($\lambda = 1.5406$ Å) of Li_2MnO_3 with $C2/m$ stacking and different percentages of stacking faults. (b) Enlargement between 20° and 35°, 2θ showing the best fit between experimental and simulated data.

faults for the $C2/m$ model, are required to model the Li_2MnO_3-1000-1m data. This is illustrated in Figs. 7b and 8b, which show the 20–35°, 2θ region. Although the simulations model the experimental data well, the Li_2MnO_3-850-1d sample appears to be more heterogeneous than implied by our model, containing both more well-ordered and more disordered regions. The observation that a higher number of faults are required to model the experimental data, for models using $C2/m$ vs. $P3_112$ stacking is ascribed to small differences in structure factors associated with the two stacking schemes. This is due to both the different packing arrangements of the two structures and the differences in symmetry. This is apparent from a simple visual inspection of the two structures shown in Fig. 1b and c. For example, the $020_{C2/m}$ (i.e., $C2/m$ indexing) reflections result from diffraction from the set of planes parallel to the mirror planes shown in (d). $C2/m$ packing clearly results in a larger structure factor for this reflection (approximately a factor of two higher), since all the Li^+ ions are located on the planes. However, the $P3_112$ space group contains a 3-fold screw axis and thus, there are three equivalent (100) planes. This results in ratios of approx. 1:0.172 ($003:020_{C2/m}$) and 1:0.202 ($003:100_{P3112}$) for the intensities of the first two observed reflections for $C2/m$ and $P3_112$ cells, respectively. Rietveld refinements of the structure and results from first principles calculations suggest that $C2/m$ stacking is a more appropriate stacking scheme, at least for Li_2MnO_3, and thus the higher numbers of stacking faults obtained from the $C2/m$ simulations should reflect the concentrations of faults present in these materials. Furthermore, the peak shapes of the $h0l_{P3112}$ reflections obtained with the $C2/m$ stacking are closer to the lineshapes seen experimentally for the Li_2MnO_3-1000-1m sample. As the disorder increases, it will eventually be impossible, and not even appropriate, to distinguish between $P3_112$ stacking and $C2/m$ stacking with rotational stacking faults (Fig. 6(b) and (c).

No large differences are seen for the 20–35°, 2θ regions between simulations made for the $C2/m$ simple stacking faults shown in Fig. 6(a), vs. stacking faults that introduce 120° rotations in the stacking (Fig. 6(a–c)). However, we have not attempted to model these stacking faults for layers with non-ideal values of β. Stacking faults that introduce these rotations are expected to result in broadening of some of the reflections at higher values of 2θ, e.g., at 45°, as observed in the experimental data of the more disordered samples. These observations are consistent with XRD simulations performed for the layered mineral Celadonite, where "rotational" vs. "translational" stacking faults could not be distinguished by XRD [20].

No hkl_{P3112} reflections should be observed in the 20–35° region for random stacking of layers. In our simulations, a weak peak remains at the same 2θ value as the $h00$ peak (0 2 0 $C2/m$ indexing) remains. An enlargement of this region (insert in Fig. 7(a)) shows a reflection with a characteristic lineshape (a Warren peak [21]) from a 2D crystal, as observed, e.g., in samples of turbostatically disordered graphite [22,23] or in $LiAl_2(OH)_7 \cdot 2H_2O$ [24].

This peak is tentatively ascribed to an hk reflection. Furthermore, this suggests that the experimentally observed broadening of the $h00$ peaks in the Li_2MnO_3-850-1d and Ni^{2+}-containing materials is due to the finite sizes of the ordered domains in the ab planes.

These results are consistent with the DFT calculations, where although the $C2/m$ structure was found to be the ground state, only small differences in energy per formula unit between the stacking schemes were observed. These small energy differences indicate a small energy penalty associated with a shifting of the transition metal stacking. Since the experimentally determined concentration of stacking faults decreases on extended annealing, the faults seen in these materials are not ascribed to thermal stacking faults but rather to disorder arising from the slow kinetics associated with ordering both in the a–b plane and in the c-direction. The growth of long-range ordering in the c-direction is expected to be particularly slow, especially given the very small energy differences between the different stacking schemes. Whether such small energy differences will lead to thermal stacking faults depends on the coherence length of the Li–Mn ordering within the transition metal layer, as this determines the size of the domain over which the fault extends and hence its total energy. Only if this *total* energy of the fault is of the order of the thermal energy can faults be stabilized by entropic effects. Hence, extremely high temperatures are likely required to increase the concentration of the thermal stacking faults in the more-well ordered materials.

Finally, the results here should be compared with our earlier single-crystal electron diffraction results [7,8]. An apparent 3-fold axis along the c-direction was seen in all the zone axes that were investigated (e.g., the $[\bar{1}\,1\,1]_{hex.}$ and $[001]_{hex.}$ zones, where the cells are indexed based on the α-$NaFeO_2$ cell (i.e., $[\bar{3}\,1\,\bar{6}]_{mon.}$ and $[103]_{mon.}$, respectively, using the $C2/m$ indexing)) [10]. The apparent 3-fold axis seen by electron diffraction, is ascribed to the 120° rotational stacking faults, which may introduce apparent 3-fold rotation axes in single crystal diffraction patterns, for appropriate concentrations of stacking faults or configurations [20]. For sufficiently thick samples and high concentrations of defects, rotational stacking faults should result in three sets of reflections with equal intensity, due to the three different unit cells related by the 3-fold screw symmetry axis. For thinner samples, or for samples with very few faults, the reflections from the three different cells may have

different intensities. Similar phenomena have been observed in other disordered layered materials. For example, in $LiAl_2(OH)_7 \cdot 2H_2O$, which contains ordered $[Li_{1/3}Al_{2/3}]$ layers, disorder in the stacking sequences leads to a hexagonal indexing of the diffraction pattern, although the structure is better described by the $C2/m$ cell [24]. Simulations of the electron diffraction data of our systems are currently in progress to explore this in more detail.

5. Conclusions

A combination of short- and long-range structural probes has been used to investigate ordering in the Li_2MnO_3–$Li[Ni_{0.5}Mn_{0.5}]O_2$ pseudo-binary. Li NMR experiments, which probe short-range order, show that the $[Li_{1/3}Mn_{2/3}]$ layers of Li_2MnO_3 are well ordered. Based on the signal-to-noise ratio of the experiments, an upper limit for Li/Mn disorder in these layers of 0.2% (Li occupancy on the Mn site) can be estimated. The NMR signals of Li ions in the Li layers, which separate the $[Li_{1/3}Mn_{2/3}]$ layers, suggest that the stacking of $[Li_{1/3}Mn_{2/3}]$ layers contains faults, particularly in the Li_2MnO_3 sample fired for a short period of time. These faults result in broadening of certain reflections ($h\,o\,l$ reflections indexed using a hexagonal cell) resulting in poor profile fits to the experimental XRD data in Rietveld refinements of the structures of these materials. Slightly lower R-factors for the refinements were obtained by allowing Li/Mn exchange in the $[Li_{1/3}Mn_{2/3}]$ layers, an approach that has been used previously in the literature; [5] this changes the absolute and relative intensities of the reflections due to the Li/Mn ordering (e.g., the $0\,2\,0_{C2/m}$ and $1\,1\,0_{C2/m}$ reflections) improving the profile fit. However, the NMR results suggest that this approach is not necessarily justified.

DIFFaX simulations of the synchrotron XRD data were performed to model the effect of stacking faults on the XRD patterns. These simulations model the line broadenings and intensity changes of the superstructure peaks arising from ordering of the $[Li_{1/3}Mn_{2/3}]$ layers and allow the concentrations of stacking faults to be estimated. The XRD data are consistent with $C2/m$ structure. The apparent 3-fold symmetry axis seen in the electron diffraction of these materials is ascribed to rotational stacking faults that result in stacking in three different directions related by the 3-fold screw axis.

Similar superstructure peaks are seen on Ni doping, the $[Li_{1/3}Mn_{2/3}]$-like ordering being better developed for lower Ni^{2+}-doping levels. Again, the XRD patterns are consistent with faults in the stacking of the layers. Even for $Li[Ni_{1/2}Mn_{1/2}]O_2$, weak superstructure peaks are seen. Our results suggest that care needs to be taken when interpreting XRD patterns of these classes of materials. Even when superstructure peaks are not observed, long-range order may still be present in the layers (i.e., in the ab plane); if there is no order, or only weak ordering of the stacking of the layers in the c-direction, the superstructure peaks will either be absent or will be very weak.

Acknowledgments

The work was supported by the Assistant Secretary for Energy Efficiency and Renewable Energy, Office of FreedomCAR and Vehicle Technologies of the US Department of Energy under Contract No. DE-AC03-76SF00098, via subcontract Nos. 6517748 and 6517749 with the Lawrence Berkeley National Laboratory. Use of the Advanced Photon Source (APS) was supported by the US Department of Energy, Office of Science, Office of Basic Energy Sciences, under Contract No. W-31-109-Eng-38. We thank Peter L. Lee for collecting the XRD data at APS and John B. Parise, Peter Stephens and Mike Treacy for helpful discussions.

Appendix A. Supplementary materials

The online version of this article contains additional supplementary data. Please visit doi:10.1016/j.jssc.2005.05.027

References

[1] T. Ohzuku, Y. Makimura, Chem. Lett. 744 (2001).
[2] Z. Lu, D.D. MacNeil, J.R. Dahn, Electrochem. Solid-State Lett. 4 (2001) A191.
[3] Z. Lu, L.Y. Beaulieu, R.A. Donaberger, C.L. Thomas, J.R. Dahn, J. Electrochem. Soc. 149 (2002) A778.
[4] J. Bréger, N. Dupré, P.J. Chupas, P.L. Lee, T. Proffen, J.B. Parise, C.P. Grey, J. Am. Chem. Soc. 127 (20) (2005) 7529.
[5] V. Massarotti, M. Bini, D. Capsoni, A. Altomare, A.G.G. Moliterni, J. Appl. Crystallogr. 30 (1997) 123.
[6] P. Strobel, B. Lambert-Andron, J. Solid State Chem. 75 (1998) 90.
[7] Y.S. Meng, G. Ceder, C.P. Grey, W.-S. Yoon, Y. Shao-Horn, Electrochem. Solid-State Lett. 7 (2004) A155.
[8] Y.S. Meng, G. Ceder, M. Jiang, J. Bréger, C.P. Grey, W.-S. Yoon, Y. Shao-Horn, Chem. Mater. 17 (9) (2005) 2386.
[9] V. Jansen, R. Hoppe, Z. Anorg. Allg. Chem. 397 (1973) 297.
[10] A. Riou, A. Lecerf, Y. Gerault, Y. Cudennec, Mater. Res. Bull. 27 (1992) 269.
[11] G. Lang, Z. Anorg. Allg. Chem. 348 (1966) 246.
[12] H. Kobayshi, M. Tabuchi, M. Shikano, H. Kageyama, R. Kanno, J. Mater. Chem. 13 (2003) 957.
[13] M.M.J. Treacy, J.M. Newsam, M.W. Deem, Proc. Roy. Soc. Lond. A 433 (1991) 499.
[14] W.-S. Yoon, N. Kim, X.Q. Yang, J. McBreen, C.P. Grey, J. Power Sources 119-121 (2003) 649.
[15] Y.J. Lee, C.P. Grey, J. Phys. Chem. B 106 (2002) 3576.
[16] K.R. Morgan, S. Collier, G. Burns, K. Ooi, J. Chem. Soc., Chem. Commun. (1994) 1719.

[17] P. Mustarelli, V. Massarotti, M. Bini, D. Capsoni, Phys. Rev. B 55 (1997) 12018.
[18] C.P. Grey, Y.J. Lee, Solid State Sci. 5 (2003) 883.
[19] A.C. Larson, R.B. Von Dreele, General structure analysis system (GSAS), Los Alamos National Laboratory Report LAUR (2000) 86–748;
B.H. Toby, J. Appl. Crystallogr. 34 (2001) 210.
[20] F. Muller, A. Plançon, G. Besson, V.A. Drits, Mater. Struct. 6 (1999) 129.
[21] B.E. Warren, Phys. Rev. 59 (1941) 693.
[22] D. Yang, R.F. Frindt, J. Appl. Phys. 79 (5) (1996) 2376.
[23] H. Shi, J.N. Reimers, J.R. Dahn, J. Appl. Crystallogr. 26 (1993) 827.
[24] J.P. Thiel, C.K. Chiang, K.R. Poeppelmeier, Chem. Mater. 5 (1993) 297.